Article:
James, AD, Moon, DR, Feng, W et al. (2017) The Uptake of HO_2 on Meteoric Smoke Analogues. Journal of Geophysical Research: Atmospheres, 122 (1). pp. 554-565. ISSN: 2169-897X

https://doi.org/10.1002/2016JD025882

The Uptake of HO_2 on Meteoric Smoke Analogues

Alexander D. James[1], Daniel R. Moon[1], Wuhu Feng[1,2], Pascale S. J. Lakey[1,3], Victoria L. Frankland[1], Dwayne E. Heard[1,2] & John M. C. Plane[1]*

1. School of Chemistry, University of Leeds, Leeds, LS2 9JT, UK
2. National Centre for Atmospheric Science, University of Leeds, Leeds, UK
3. Max Planck Institute for Chemistry, Hahn-Meitner-Weg 1, 55128 Mainz

* Corresponding author: j.m.c.plane@leeds.ac.uk, +44 113 3438044

For submission to the Journal of Geophysical Research - Atmospheres

Abstract

The kinetics of heterogeneous HO_2 uptake onto Meteoric Smoke Particles (MSPs) has been studied in the laboratory using analogues of MSP aerosol entrained into a flow tube. The uptake coefficient, γ, was determined on synthetic amorphous olivine ($MgFeSiO_4$) to be $(6.9 \pm 1.2) \times 10^{-2}$ at a relative humidity (RH) of 10%. On forsterite (Mg_2SiO_4), $\gamma = (4.3 \pm 0.4) \times 10^{-3}$ at RH = 11.6%, and $(7.3 \pm 0.4) \times 10^{-2}$ at RH = 9.9% on fayalite (Fe_2SiO_4). These results indicate that Fe plays a more important mechanistic role than Mg in the removal of HO_2 from the gas phase. Electronic structure calculations show that Fe atoms exposed at the particle surface provide a catalytic site where HO_2 is converted to H_2O_2 *via* an Eley-Rideal mechanism, but this does not occur on exposed surface Mg atoms. The impact of this heterogeneous process in the middle atmosphere was then investigated using a whole atmosphere chemistry-climate model which incorporates a microphysical treatment of MSPs. Using a global MSP production rate from meteoric ablation of 44 tons per day, heterogeneous uptake (with $\gamma = 0.2$) on MSPs significantly alters the HO_x budget in the night-time polar vortex. This impact is highly latitude dependent and thus could not be confirmed using currently available satellite measurements of HO_2, which are largely unavailable at latitudes greater than 70°.

Introduction

A significant discrepancy exists between observations and model predictions of HO_2 concentrations in the middle atmosphere, known as the 'HO_x dilemma' [*Millán et al.*, 2015]. *Siskind et al.* [2013] showed that increasing the rate coefficient for the reaction

$$H + O_2 (+ M) \rightarrow HO_2, \text{ where } M = N_2 \text{ or } O_2 \quad (1)$$

by a factor of ~1.5 improved agreement to the observed OH profile, but did not present a detailed comparison for HO_2. *Pickett et al.* [2008] found that for northern hemisphere summer, rate constants within the stated error of the JPL 2006 recommendation could explain the observed HO_2 but did not discuss other seasons or latitudes. In general, a kinetic description which underpredicts HO_2 density in the upper mesosphere results in over-prediction in the lower mesosphere / stratosphere and *vice versa* [*Millán et al.*, 2015].

The modelling studies discussed above consider only gas-phase chemistry. In terms of heterogeneous chemistry, noctilucent clouds occur in the polar summer mesosphere above 80 km, causing perturbations to atomic O and HO_x around the ice clouds [*Murray and Plane*, 2005]. However, in the middle mesosphere below 80 km the only known source of potentially reactive surfaces are Meteoric Smoke Particles (MSPs). These particles form by recondensation of the metallic vapours which are released by meteoric ablation [*Hunten et al.*, 1980; *Plane et al.*, 2015] and are likely composed of Fe-Mg-silicates [*Saunders and Plane*, 2006]. Recent studies have shown that uptake on MSPs may significantly affect the atmospheric abundance of species such as HNO_3 and H_2SO_4 in the stratosphere/lower mesosphere [*Frankland et al.*, 2015; *Saunders et al.*, 2012]. The heterogeneous recombination of O and H_2 on MSPs has also been suggested as a source of H_2O in the lower mesosphere [*Summers and Siskind*, 1999].

A study of the heterogeneous chemistry of HO_2 on MSPs is therefore timely. Here we report an experimental measurement of the uptake coefficient, γ, for HO_2 on a variety of MSP analogues, which were prepared using a sol-gel process that we have described previously [*Frankland et al.*, 2015]. The uptake rate was measured by entraining these particles in a laminar gas flow, and detecting HO_2 by conversion to OH and the Fluorescence Assay by Gas Expansion (FAGE) technique [*Matthews et al.*, 2014].

The Fluorescence Assay by Gas Expansion (FAGE) technique is used to detect HO_2 radicals with very high sensitivity, building from extensive experience in measuring these radicals in the field [*Stone et al.*, 2012]. Briefly, gas is sampled at the end of the aerosol flow-tube by a small circular pinhole (diameter 0.7 mm), at which point the gas expands supersonically into a low pressure fluorescence cell, and the gas jet is crossed by a laser beam ~ 120 mm from the pinhole. The background pressure in the cell is held at ~ 1 Torr, with the fast flow of gas maintained by a rotary pump/roots blower combination, and close to the pinhole nitric oxide (NO, 99.5.%, BOC) is added to convert HO_2 to OH radicals, which are detected by laser-induced fluorescence exciting at a wavelength of ~308 nm (from a high pulse-repetition-frequency Nd: YAG pumped dye laser) using the $Q_1(2)$ rotational transition of the $A^2\Sigma$ (v′=0) - $X^2\Pi_{3/2}$ (v″=0) vibronic band of OH. On-resonant fluorescence is collected *via* the same band, using a series of fast lenses and an interference filter centred at 308 nm, and in order to discriminate against the more intense laser scattered light, the fluorescence, whose lifetime is extended at the low pressure, is detected *via* delayed photon counting. The detector (Perkin Elmer 993P) is gated off during the laser-pulse to avoid saturation from the scattered light. The sensitivity of the HO_2 detection is calibrated using a known concentration of HO_2 generated from the photolysis of water vapour at 185 nm in presence of zero air (Whalley et al., 2011, George et al., 2013, Matthews et al., 2014), and is ~ 10^6 molecule cm^{-3}.

A version of the Whole Atmosphere Community Climate Model (WACCM) coupled with the Community Aerosol and Radiation Model for Atmospheres (CARMA) which includes a treatment of MSP microphysics [*Bardeen et al.*, 2008], was then used in order to determine if MSPs can have an impact on the HO_x budget. Because of uncertainties in the uptake coefficients this study does not attempt to quantify any such impact. Rather the modelling presented here is intended to give the reader an idea of when and where such an impact might occur.

Experimental Method

MSP analogues in the form of amorphous compounds with olivine compositions $Mg_xFe_{2-x}SiO_4$ (where $0 \leq x \leq 2$) were produced by mixing stoichiometric quantities (relative to 0.1 molar product) of aqueous solutions of magnesium chloride (Aldrich), ferrous (II)

ammonium sulfate (Sigma-Aldrich) and sodium orthosilicate (Alfa Aesar) at room temperature for 7 days [*Frankland et al.*, 2015]. Metal-salt by-products were removed from products by repeated dialysis using a soxhlet apparatus with the particles held in water-permeable tubing (Snakeskin 7000 MWCO). This method was used to produce materials with x = 0, 1 and 2. Although the products are amorphous, they will hereafter be referred to respectively as fayalite, olivine and forsterite for simplicity.

The experimental procedure for measuring the HO_2 uptake coefficients has been described in detail elsewhere [*George et al.*, 2013; *Matthews et al.*, 2014]. An experimental diagram is shown in Figure 1.

Details of the gas flow control system are given in *Matthews et al.* [2014] which described uptake experiments onto Arizona Test Dust aerosols. The carrier gas used for these experiments was compressed nitrogen which first passed through a gas purification system consisting of particle filters, a dryer and a carbon filter. The HO_2 flow, the humidified flow and the NO flow were controlled using five mass flow controllers (Brooks, model 5850S and MKS, model 1179A). The required Relative Humidity (RH) was obtained by mixing together and altering the ratio of a dry flow and a flow which had been passed through a water bubbler (Milli-Q, 18 MΩ cm). This humidified flow, which was mixed with the aerosol flow in the conditioning flow tube, was ~ 3 litres per minute (lpm) throughout each individual experiment. The aerosol flow was monitored and maintained at 1.0 ± 0.1 lpm and the HO_2 flow from the injector (which is moved to provide varied contact times in random order) was measured as 1.3 ± 0.05 lpm. The total flow passing through the flow tube (with 5.9 cm diameter), including the aerosol, dilution and HO_2 flows, was ~5.3 ± 1 lpm (variations are due to the mixing of dry and humid flows). The FAGE instrument sampled ~ 4.2 lpm and the Condensation Particle Counter (CPC, TSI 3775) sampled 0.3 lpm with the remainder of the flow (~0.8 lpm) exiting *via* an exhaust line. The pressure and temperature in the aerosol flow-tube were maintained at atmospheric pressure and room temperature (~20-22^{o}C).

MSP aerosols were entrained in the carrier gas using either a magnetic stirrer (shown in Figure 1) or acoustic dust disperser and passed through an impactor (TSI 1034900, nozzle diameter 0.71 mm, D_{50} = 1286 nm), which was used to stabilise the flow rate from the dust disperser. The concentration of aerosols entering the flow tube was controlled using a High Efficiency Particulate Air (HEPA) filter and a bypass. The proportion of the flow passing

130 through the bypass compared to the filter was controlled using a needle valve (not shown in
131 Figure 1). The aerosol number concentration was monitored using a CPC. Measurements
132 were also made either immediately before or after each uptake experiment, under the same
133 experimental conditions, using a Scanning Mobility Particle Sizer (SMPS, TSI, 3080) in order
134 to measure the entire log normal size distribution. Checks determined that the average
135 radius did not change over time or when sampling from before or after the flow tube. The
136 size distribution was independent of whether HO_2 was flowing from the injector or not.

137 HO_2 was formed by passing water vapour in front of a mercury pen-lamp to form OH and H;
138 HO_2 is then produced when the latter reacts with trace O_2 impurity in the N_2 carrier gas. This
139 produces an initial HO_2 concentration in the second flow tube of 1.6×10^9 molecules cm^{-3}.
140 Variability in the HO_2 signal due to lamp output and supplied humidity (controlled by flow
141 controllers) is very small. The absolute concentration downstream is known following
142 calibration of the sensitivity of the fluorescence cell [*George et al.*, 2013]. The injector was
143 used to vary the contact time of the HO_2 with the aerosol to determine the uptake kinetics.
144 Experiments were performed on all 3 MSP analogue materials.

145 **Results and Discussion**

146 ***Measured size distributions***

147 A typical set of 10 measured size distributions is shown for fayalite at 9.9 % RH in Figure 2.
148 The mean, which is used to calculate the experimental surface area, is shown in black. This
149 shows that, while there is some variability in the output of the aerosoliser, a log normal
150 distribution is measured and can be well characterised (in this case the distribution had a
151 mean of 368 nm and a standard deviation of 0.680). This gives a measurement of the mean
152 surface area of each MSP (4.25×10^{-9} cm^2 in this example). CPC measurements of the
153 number concentration are used during experiments to calculate the total available surface
154 area.

155 The spherical assumption used here for the particles neglects any surface roughness and
156 may lead to an underestimation of the surface area available for HO_2 to interact with. This
157 would result in an overestimation of the uptake coefficient [*Frankland et al.*, 2015].

Measurements of the uptake coefficient,

A clear uptake of HO_2 to the MSP analogues was observed in all experiments. Figure 3 (a) illustrates the relationship between the fayalite aerosol number concentration and HO_2 signal in a typical experiment where the RH was 9.9 % and residence time of 20.6 s. Raw HO_2 signal is shown. Before further analysis the data were corrected for the output power of the laser. The reference cell signal would also enable any drifts in laser power or wavelength to be monitored, and is used to centre the laser wavelength on the OH transition. If the reference cell changes significantly (but not the laser power) then the data are not used so the laser power is considered a good reference for normalisation. Since uptake is a first-order process, the HO_2 concentration $[HO_2]_t$ is then related kinetically to the available aerosol surface and the initial concentration $[HO_2]_0$ by

$$-\ln\frac{[HO_2]_t}{[HO_2]_0} = 0.25\gamma_{obs}wA_dN_dt + k_Wt \quad \text{(E1)}$$

where γ_{obs} is the observed uptake coefficient, w the molecular mean speed (cm s^{-1}), N_d the number density of aerosol (cm^{-3}), A_d the surface area of the mean aerosol particle (cm^2), t the contact time (s) during which HO_2 can adsorb onto the particles, and k_w the rate coefficient for loss (s^{-1}) of HO_2 on the flowtube walls and by self-recombination in the gas-phase to form H_2O_2. This is determined by measuring uptake without the aerosol flow for several injector positions at the beginning and end of each experiment (under the same RH conditions). It should be noted that at HO_2 concentration of ~10^9 molecule cm^{-3} the loss via the gas phase reaction is very small (e-folding lifetime >100 s). At the pressure of 1 bar used in these experiments, diffusional transport of HO_2 to the particle surface is not in the free molecular regime, so γ_{obs} was then corrected for slip flow [*Matthews et al.*, 2014]:

$$\gamma = \frac{\gamma_{obs}}{1-\gamma_{obs}\lambda(r_s)} \quad \text{(E2)}$$

where $\lambda(r_s)$, the mean free path for a particle of radius r_s, is given by

$$\lambda(r_s) = \frac{0.75+0.28Kn}{Kn(1+Kn)} \quad \text{(E3)}$$

where Kn, the Knudsen number, is given by

$$Kn = \frac{3D_g}{wr_s} \quad \text{(E4)}$$

and D_g is the diffusion constant for HO_2, taken to be 0.25 $cm^2\ s^{-1}$ at 1 bar [*Mozurkewich et al.*, 1987]. This results in a range of *Kn* from 1.26 for the smallest to ~0.3 for the largest particles. The contact time *t* was determined for the experimental flow conditions (Reynolds number = 136) by applying the Brown correction to the plug flow time determined from the mass flow rates and pressure [*Brown*, 1978]. Figure 3 (b) shows that $\ln[HO_2]_t$ was linearly anti-correlated with N_d, in accord with equation (E1), so the slope is equal to $0.25\gamma_{obs}wA_dt$ ($(6.3 \pm 1.4) \times 10^{-6}$ in this case). The slope was then measured over a range of contact times and found to vary linearly as shown in Figure 4 (a) (for fayalite at RH of 9.9 %, R^2=0.945). The mean aerosol surface area determined from a log-normal fit to the SMPS data and the gradient of the line in Figure 4 (a) was used to determine γ.

Matthews et al. [2014] suggested that a positive intercept on a plot such as Figure 4 (a) can be indicative of some experiments occurring at contact times too short for HO_2 to reach equilibrium with the surface. By plotting a line from the origin to each point in Figure 4 (a), the change in uptake coefficient over time can be quantified. This is shown in Figure 4 (b). Some surface sites in these experiments appear to be deactivated as the HO_2 comes to equilibrium with the MSP analogues. The probability of uptake is less at equilibrium (when some sites are occupied) than for surfaces which have had contact times too short to reach equilibrium. Note that the uptake coefficient at long times approaches that calculated from the fit to the whole data set. These values should be taken as the true measurement of uptake, since they correspond to HO_2 in equilibrium with the surface. Any change in the system as a result of the experimental process, *e.g*. deposition of analogue particles in the flow tube, could also lead to changes in the intercept of plots such as Figure 4 (a) but since the measurements at different contact times are performed in random order this could not explain the observed larger uptake coefficients for points at shorter contact times.

Surface coverage of HO_2 can be further investigated by estimating the mean distance between HO_2 molecules on the surface at the longest contact times, assuming that all HO_2 which are taken up remain on the surface. This is done by integrating the loss of HO_2 with respect to time to determine the total adsorbed on dust of known surface area, and assuming the HO_2 molecules are dispersed isentropically over the surface. The smallest distance estimated here was 10 Å, implying that a significant proportion of the surface sites might have become saturated. However, the linearity of plots such as those shown in

Figures 4 (a) implies that there was no deviation from constant first-order uptake kinetics. This suggests that HO_2 is converted to other products and many of the available surface sites are re-activated. This is discussed further in the light of electronic structure calculations below.

Matthews et al. [2014] also found that the uptake coefficient decreased by a factor of two with a four fold increase in the initial concentration of HO_2. Since the mechanism in both cases is likely driven by Fe active sites [*Broadley et al.*, 2012], we would expect a similar trend here. Equivalent experiments, which are technically challenging and cannot cover a large range of $[HO_2]_0$, were therefore not performed in this study. γ values measured in this study are summarised in Table 1. The larger γ values measured on olivine and fayalite suggest that HO_2 is taken up more readily by Fe compared with Mg active sites on the MSP analogue surface.

A number of previous studies have concluded that HO_2 uptake could be driven by the presence of Transition Metal Ions (TMIs) at the particle surface or in the bulk of a liquid particle eg. [*Lakey et al.*, 2015]. *Mao et al.* [2013] demonstrated that where Fe and Cu ions are both present in a liquid droplet redox chemistry can lead to the production of H_2O rather than H_2O_2. These mechanisms are not likely to be important here, however, since for TMIs to be available in a liquid droplet would require both RH approaching 100% and a soluble solid. Since by-products of the synthesis process are removed from the MSP analogues by repeated dialysis in near boiling point water, it is unlikely that any soluble material remains.

Electronic structure calculations

In order to investigate the mechanism for HO_2 uptake on the MSP analogue surfaces, we employed electronic structure calculations using the Gaussian 09 suite of programs [*Frisch et al.*, 2009]. The hybrid density functional/Hartree-Fock B3LYP method was employed together with the 6-311+G(2d,p) triple zeta basis set, which is a reasonably large, flexible basis set with both polarization and diffuse functions added to the atoms. We have used this level of theory previously for calculations on Fe- and Mg-containing oxides, hydroxides and silicates [*Rapp et al.*, 2012; *Saunders and Plane*, 2011]. The expected uncertainty in the calculated reaction enthalpies is ±20 kJ mol^{-1} at this level of theory.

Since we are interested in the reactivity of HO_2 with exposed surface sites, here we consider the binding of HO_2 to either the Fe or Mg end of an $FeMgSiO_4$ unit. While this is clearly an approximation of the surface, it yields useful insights into the likely mechanisms that occur and is useful for interpreting the experimental observations. For each molecule the geometry was first optimised, and then vibrational frequencies calculated to determine the zero point energy correction. The most stable form of $FeMgSiO_4$ has quintet spin multiplicity [*Saunders and Plane*, 2011] because of the presence of the Fe atom. We therefore considered all possible spin multiplicities of the species involved in HO_2 uptake and subsequent reaction. The results for the most stable spin states are reported here (though in fact the different states of the relevant molecules are near-degenerate).

These calculations indicate that an exposed surface Fe atom is able to catalyse the destruction of HO_2 *via* the overall reaction

$$HO_2 + HO_2 \rightarrow H_2O_2 + O_2 \qquad (2)$$

Figure 5 illustrates the catalytic mechanism. An HO_2 first chemisorbs to the Fe atom with a substantial binding energy of 225 kJ mol^{-1} (Figure 4(a) and (b)). A second HO_2 can then abstract the adsorbed H atom, in a reaction that is quite exothermic (ΔH^o(0 K) = -77 kJ mol^{-1}). Note that the differing role of the two HO_2 radicals effectively makes the reaction first order, reconciling this mechanism with the kinetic plots shown above. This reaction occurs *via* a submerged transition state (Figure 4(c)) to yield H_2O_2 and an O_2 molecule bound to the Fe atom (Figure 4(d)). Finally, a third HO_2 can displace the bound O_2 exothermically (ΔH^o(0 K) = -64 kJ mol^{-1}) to yield the structure in Figure 4(b), hence starting the Eley-Rideal cycle over again.

In contrast, when HO_2 adsorbs onto an exposed Mg, the H atom migrates onto an O of the silicate group and the remaining O_2 is strongly bound to the Mg (Figure 4(e)). This process is even more exothermic than adsorption to the Fe, with ΔH^o(0 K) = -342 kJ mol^{-1}. However, the H atom cannot be abstracted *via* a gas-phase HO_2, because this is highly endothermic (ΔH^o(0 K) = 106 kJ mol^{-1}), and the O_2 is too strongly bound to the Mg atom to be displaced. Thus the adsorption effectively deactivates the Mg site.

These calculations therefore provide an explanation for two experimental observations: the much larger value of γ for fayalite compared with forsterite; and the fact that the uptake rate on olivine and fayalite reach a steady state at large contact times.

Atmospheric modelling

In order to explore the impact of HO_2 uptake on MSPs, we have used WACCM (extending vertically from the surface to 140 km) coupled with the CARMA aerosol microphysics model [*Marsh et al.*, 2013]. This combination has previously been used by *Bardeen et al.* [2008] to treat MSPs in the atmosphere and by *Frankland et al.* [2015] to examine the effect of uptake to MSPs on the HNO_3 budget. A cosmic dust input rate into the atmosphere of 44 tons day^{-1} is used, and this all assumed to ablate and subsequently form MSPs. Model simulations for the years 2004 – 2010 were carried out with specified dynamics using a meteorological data set from Goddard Earth Observing System model (GEOS) 5 below 50 km. Dynamics were specified as in *Feng et al.* [2013], so that 1% of the meteorological conditions (temperature, winds, surface pressure, specific humidity, surface wind stress, latent, sensible heat flux, etc.) were combined with the WACCM fields below 50 km at every model dynamics time step. This nudging factor then reduced linearly from 1 to 0 % between 50-60 km. Above 60 km there is no nudging to the re-analysis fields and the model in this region is free-running. Two WACCM-CARMA simulations were run: a control experiment with no uptake of HO_2 to MSPs, and a second experiment where removal was added using γ = 0.2. Comparison of the 2 runs then allows assessment of the importance of this process.

This study aims to demonstrate an impact of MSP on the atmospheric availability of HO_2 in terms of when and where an impact would be observable. Quantification of such an impact is not an aim since uncertainties in the uptake coefficient are both too large and too complex [*Frankland et al.*, 2015]. The available surface area of MSP is also uncertain, both in terms of the total mass influx and the fractal agglomerate nature of the atmospheric particles [*Plane*, 2012; *Saunders et al.*, 2007].

An uptake coefficient (see equation E5, below) for the atmospheric modelling was chosen as follows. Recent measurements have shown that HO_2 uptake tends to be more rapid for higher RH (See Figure 3 in *Lakey et al.* [2015] and Figure 6 in *Matthews et al.* [2014]). This is either due to dissolution of TMI (although note that as droplet size increases the

concentration of TMI decreases so that the uptake would begin to reduce again in large droplets) or a $HO_2.H_2O$ complex may form on the surface and react more rapidly than HO_2 radicals in a similar mechanism to that proposed for the gas phase [*Stone and Rowley*, 2005]. Although the middle atmosphere is relatively dry, significant RH can be reached at low temperatures. This occurs both in the summer mesosphere, where RH exceeds 100 % and polar mesospheric ice clouds can form [*Murray and Jensen*, 2010], and in the winter stratosphere where RH can reach 20 %. This is demonstrated below in Figure 7 (b), where the RH from the WACCM control run is shown zonally averaged at 80° S as a function of pressure and time. For the most part, however, the middle atmosphere is significantly dryer than it is possible to measure using the current apparatus since H_2O is required to produce HO_2. Nevertheless, as the ambient conditions move toward low RH a kinetic steady state will be reached where a mechanism not involving H_2O will dominate. This will cause the uptake coefficient to stabilise, as seen for example in measurements on humic acid (Figure 3 in *Lakey et al.* [2015]). The uptake coefficient of ~0.07 measured here on olivine and fayalite likely holds for lower RH at room temperature. At colder atmospheric temperatures this is likely to increase [*Mao et al.*, 2010]. Measuring γ at other atmospheric temperatures was not possible with the apparatus used in this study, however it has been noted that γ usually increases with decreasing temperature [*Hayward et al.*, 1967].

γ=0.2 has therefore been used in the WACCM-CARMA model. This is a physically reasonable value (γ as high as 0.8 have been measured in the past for HO_2 uptake on aqueous aerosol [*Thornton and Abbatt*, 2005]). Such high values have previously been measured on solid aerosols only when significant Cu is present, however Fe and other transition metals are also known to take up HO_2 efficiently [*Mao et al.*, 2010].

There is considerable uncertainty in the total amount of cosmic dust entering the atmosphere each day [*Rapp et al.*, 2012], and the fraction that ablates is a function of the dust size and velocity distributions. Hence it is possible that the value of the ablated mass input is higher by up to a factor of 3 [*Carrillo-Sánchez et al.*, 2015], which would result in a larger modelled impact of MSP on the HO_2 abundance. Besides the uncertainty in the total MSP mass *Saunders et al.* [2007] showed that MSPs likely consist of fractal chain aggregates which would imply that the surface area they present for reaction would be significantly higher than the spherical approximation used in the current modelling scheme. MSP were

input to WACCM-CARMA simulations as 0.2 nm radius primary particles (approximately molecular dimensions) injected over a range of altitudes between 75 and 110 km, with the peak injection rate at 83 km. Particles were then allowed to agglomerate collisionally and the surface area calculated in each model time step.

The rate of uptake to an atmospheric aerosol is defined by

$$\frac{d[HO_2]}{dt} = -0.25 w \gamma A_d [HO_2] \quad \text{(E5)}$$

where A_d (cm^2 cm^{-3}) is the volumetric surface area of aerosol available in the atmosphere. Note that (E1) is the solution to an equation of a similar form to (E5) but differs in that the former must account for losses, both to the flow tube walls and through gas phase self-recombination, and considers a mean aerosol particle. In addition at the low pressures (uptake in the model occurs at pressures below 5 hPa, see below) present in the middle atmosphere the effect of diffusion can be neglected.

To assess the validity of this modelling approach, WACCM-CARMA output for the run with no HO_2 uptake to MSPs was then compared to atmospheric observations from the Microwave Limb Sounder (MLS data version 4.2x), a radiometer aboard the Aura satellite [*Livesey et al.*, 2013; *Pickett et al.*, 2008; *Waters et al.*, 2006]. All WACCM-CARMA data has been sampled at the averaging kernels used for the MLS data. This reduced the model altitude resolution in the stratosphere but allows a like with like comparison. A comparison for January 2005 is shown in Figure 6. The altitude range of both data sets has been displayed only to the recommended scientifically valid range of the MLS data (22 - 0.046 hPa, ~30 - 60 km). This is also a reasonable restriction to the WACCM-CARMA data as above this altitude nudging to the specified dynamics is not applied, whilst below this MSPs will be entrained in liquid sulfuric acid droplets and unable to take up HO_2. The comparison in general is satisfactory: the HO_2 mixing ratio increases with altitude and is fairly uniform across mid latitudes. The reduction and increase in the winter and summer polar regions, respectively, are well reproduced by the model.

WACCM-CARMA does appear to under predict the mixing ratio at the higher altitudes (around 0.05 hPa) and over predict at lower altitudes (around 5 hPa). A similar under estimation at high altitude was observed by *Millán et al.* [2015], who made an extensive comparison of WACCM to an offline retrieval of MLS HO_2 mixing ratio which was able to

365 cover a larger range of altitudes than the data used here. The authors in that study
366 speculated that either our understanding of mesospheric chemistry is incomplete, or that
367 parameterisations of solar flux may be inaccurate. *Millán et al.* [2015] did not observe the
368 over estimation at lower altitudes shown here, however this may not be present in the
369 more advanced offline HO_2 retrieval used in that study. A more thorough discussion of such
370 model discrepancies is beyond the scope of this study. Since the model broadly reproduces
371 the observations, it is deemed a useful tool for assessing the impact of heterogeneous
372 chemistry on the HO_2 abundance.

373 Figure 7 (a) illustrates the percentage difference in HO_2 volume mixing ratio, zonally
374 averaged at 80^o S and plotted against time and altitude, between the WACCM run with HO_2
375 uptake and the control run. For comparison, the % RH and MSP surface area, both from the
376 control run, are shown for the same region in Figure 7 (b & c, respectively). This
377 demonstrates a clear impact on the HO_2 profile. As stated above, because of the
378 uncertainties in both the uptake coefficient (due to temperature and RH) and surface area
379 (due to the mass input and fractal nature of particles) the aim of this study is not to quantify
380 such an impact but rather to demonstrate that it is potentially significant and where and
381 when it would most likely be observed. The latitude variation of that impact is shown for
382 June 2009 in Figure 8. The strong impact (>40% removal) near the pole falls off rapidly
383 toward mid latitudes, with less than 10% removal at all altitudes by 65^o S. This trend is
384 qualitatively reasonable even in light of uncertainty in the uptake coefficient, since it reflects
385 the downward transport of MSPs in the polar vortex.
386 Detection of the heterogeneous removal of HO_2 in the satellite observations is difficult for
387 two reasons. First, although a 40% removal is significant, the effect is only present during
388 the polar night (when background concentrations are relatively low) and thus difficult to
389 identify unambiguously. Second, there is a paucity of MLS-AURA measurements at very high
390 latitudes, where the impact of MSPs is greatest. In the future, improved datasets e.g. *Millán*
391 *et al.* [2015] may facilitate a more quantitative study. Nevertheless, the clear potential for
392 MSPs to influence the atmospheric HO_2 profile has implications for future modelling of
393 chemistry in the middle atmosphere.

Conclusions

HO_2 uptake to MSP analogues has been studied using a combination of laboratory techniques and atmospheric modelling. A dependence on the composition of the MSP analogue was observed. This appears to be a result of mechanistic and energetic differences between the binding of HO_2 to Fe and Mg sites. Uptake coefficients, γ, of $(4.3 \pm 0.4) \times 10^{-3}$, $(6.9 \pm 1.2) \times 10^{-2}$ and $(7.3 \pm 0.4) \times 10^{-2}$ were measured on forsterite, olivine and fayalite, respectively, all at RH of ~10 %.

A value for the uptake coefficient of 0.2, based on the laboratory measurements and taking into account the likely temperature and RH dependencies of γ, was applied along with a total meteoric input of 44 tons day^{-1} in WACCM-CARMA. Comparison to a control run showed that there was a significant impact on the HO_2 budget in the polar vortex, with reductions in the HO_2 volume mixing ratio of up to 40%. This impact was found to be strongly dependant on latitude, in agreement with the presence of MSPs in the polar night.

The result of the global modelling presented here should not be considered quantitatively since uncertainties in the uptake coefficient and available surface area of MSP have necessitated a rather simplistic approach. The potential for the meteoric input to be higher and the neglect of any temperature dependence of the uptake imply that this could be a lower limit to the impact of this process in the atmosphere, however the further complications of composition and humidity dependence could offset this. Future re-analysis of MLS-aura HO_2 measurements may facilitate a more quantitative comparison by extending the latitude range covered.

Acknowledgements

This work was supported by funding from the European Research Council (project number 291332 - CODITA). DM is grateful to the Natural Environment Research Council for the provision of a PhD studentship. The authors acknowledge helpful discussions with Dr Charles Bardeen (NCAR, Boulder, CO) regarding the CARMA model. The MLS data was obtained from the NASA Goddard Earth Sciences Data and Information Services Center via ftp://acdisc.gsfc.nasa.gov/data/s4pa/Aura_MLS_Level2. The source codes and input data for the standard WACCM/CARMA model (CESM version 1.1.1 used in this paper) are available from https://svn-ccsm-release.cgd.ucar.edu/model_versions/cesm1_1_1 upon registration.

The GEOS5 meteorological analyses are available at https://www.earthsystemgrid.org/home.html. The WACCM data sets are archived on a University of Leeds networked server for Plane's group and available upon request to JMCP or WF. The experimental data is available upon request to DEH.

References

Bardeen, C. G., O. B. Toon, E. J. Jensen, D. R. Marsh, and V. L. Harvey (2008), Numerical simulations of the three-dimensional distribution of meteoric dust in the mesosphere and upper stratosphere, *J. Geophys. Res.*, *113*, art. no. D17202

Broadley, S. L., B. J. Murray, R. J. Herbert, J. D. Atkinson, S. Dobbie, T. L. Malkin, E. Condliffe, and L. Neve (2012), Immersion mode heterogeneous ice nucleation by an illite rich powder representative of atmospheric mineral dust, *Atmos. Chem. Phys.*, *12*(1), 287-307

Brown, R. L. (1978), Tubular flow reactors with 1st-order kinetics, *J. Res. Nat. Bur. Stand.*, *83*(1), 1-8

Carrillo-Sánchez, J. D., J. M. C. Plane, W. Feng, D. Nesvorný, and D. Janches (2015), On the size and velocity distribution of cosmic dust particles entering the atmosphere, *Geophys. Res. Lett.*, *42*(15), 6518-6525

Feng, W., D. R. Marsh, M. P. Chipperfield, D. Janches, J. Höffner, F. Yi, and J. M. C. Plane (2013), A global atmospheric model of meteoric iron, *J. Geophys. Res.*, *118*(16), 9456-9474

Frankland, V. L., A. D. James, W. Feng, and J. M. C. Plane (2015), The uptake of HNO_3 on meteoric smoke analogues, *J. Atmos. Sol. Terr. Phys.*, *127*, 150-160

Frisch, M. J. E. A., G. W. Trucks, H. B. Schlegel, G. E. Scuseria, M. A. Robb, J. R. Cheeseman, G. Scalmani, V. Barone, B. Mennucci, and G. A. Petersson (2009), Gaussian 09, Revision A. 01, Gaussian, *Inc., Wallingford, CT*, *200*

George, I. J., P. S. J. Matthews, L. K. Whalley, B. Brooks, A. Goddard, M. T. Baeza-Romero, and D. E. Heard (2013), Measurements of uptake coefficients for heterogeneous loss of HO_2 onto submicron inorganic salt aerosols, *Phys. Chem. Chem. Phys.*, *15*(31), 12829-12845

Hayward, D. O., D. A. King, and F. C. Tompkins (1967), Variation of sticking probabilities with temperature and coverage, and desorption spectra for nitrogen on tungsten films, *Proc. Roy. Soc. Lond. A 297*(1450), 321-335

Hunten, D. M., R. P. Turco, and O. B. Toon (1980), Smoke and dust particles of meteoric origin in the mesosphere and stratosphere, *J. Atmos. Sci.*, *37*(6), 1342-1357

Lakey, P. S. J., I. J. George, L. K. Whalley, M. T. Baeza-Romero, and D. E. Heard (2015), Measurements of the HO_2 uptake coefficients onto single component organic aerosols, *Env.l Sci. Tech.*, *49*(8), 4878-4885

Livesey, N. J., et al. (2013), Earth Observing System (EOS) Aura Microwave Limb Sounder (MLS) version 4.2 level 2 data quality and description document,, edited by JPL, Jet Propulsion Laboratory, California Institute of Technology, Pasadena, California, USA,

462 Mao, J., S. Fan, D. J. Jacob, and K. R. Travis (2013), Radical loss in the atmosphere from Cu-Fe
463 redox coupling in aerosols, *Atmos. Chem. Phys.*, *13*(2), 509-519

464 Mao, J., et al. (2010), Chemistry of hydrogen oxide radicals (HO_x) in the Arctic troposphere in
465 spring, *Atmos. Chem. Phys.*, *10*(13), 5823-5838

466 Marsh, D. R., M. J. Mills, D. E. Kinnison, J.-F. Lamarque, N. Calvo, and L. M. Polvani (2013),
467 Climate change from 1850 to 2005 simulated in CESM1(WACCM), *J. Climate*, *26*(19), 7372-
468 7391

469 Matthews, P. S. J., M. T. Baeza-Romero, L. K. Whalley, and D. E. Heard (2014), Uptake of HO_2
470 radicals onto Arizona test dust particles using an aerosol flow tube, *Atmos. Chem. Phys.*,
471 *14*(14), 7397-7408

472 Millán, L., S. Wang, N. Livesey, D. Kinnison, H. Sagawa, and Y. Kasai (2015), Stratospheric and
473 mesospheric HO_2 observations from the Aura Microwave Limb Sounder, *Atmos. Chem.*
474 *Phys.*, *15*(5), 2889-2902

475 Mozurkewich, M., P. H. McMurry, A. Gupta, and J. G. Calvert (1987), Mass accommodation
476 coefficient for HO_2 radicals on aqueous particles, *J. Geophys. Res.*, *92*(D4), 4163-4170

477 Murray, B. J., and E. J. Jensen (2010), Homogeneous nucleation of amorphous solid water
478 particles in the upper mesosphere, *J. Atmos. and Sol. Terr. Phys.*, *72*(1), 51-61

479 Murray, B. J., and J. M. C. Plane (2005), Modelling the impact of noctilucent cloud formation
480 on atomic oxygen and other minor constituents of the summer mesosphere, *Atmos. Chem.*
481 *Phys.*, *5*(4), 1027-1038

482 Pickett, H. M., B. J. Drouin, T. Canty, R. J. Salawitch, R. A. Fuller, V. S. Perun, N. J. Livesey, J.
483 W. Waters, R. A. Stachnik, and S. P. Sander (2008), Validation of aura microwave limb
484 sounder OH and HO_2 measurements, *J. Geophys. Res.*, *113*, art. no. D16S30

485 Plane, J. M. C. (2012), Cosmic dust in the Earth's atmosphere, *Chem. Soc. Rev.*, *41*(19), 6507-
486 6518

487 Plane, J. M. C., W. Feng, and E. C. M. Dawkins (2015), The mesosphere and metals:
488 Chemistry and changes, *Chem. Rev.*, *115*(10), 4497-4541

489 Rapp, M., J. M. C. Plane, B. Strelnikov, G. Stober, S. Ernst, J. Hedin, M. Friedrich, and U. P.
490 Hoppe (2012), In situ observations of meteor smoke particles (MSP) during the Geminids
491 2010: constraints on MSP size, work function and composition, *Ann. Geophys.*, *30*(12), 1661

492 Saunders, R. W., S. Dhomse, W. S. Tian, M. P. Chipperfield, and J. M. C. Plane (2012),
493 Interactions of meteoric smoke particles with sulphuric acid in the Earth's stratosphere,
494 *Atmos. Chem. Phys.*, *12*(10), 4387-4398

495 Saunders, R. W., P. M. Forster, and J. M. C. Plane (2007), Potential climatic effects of
496 meteoric smoke in the Earth's paleo-atmosphere, *Geophys. Res. Lett.*, *34*, art. no. L16801

497 Saunders, R. W., and J. M. C. Plane (2006), A laboratory study of meteor smoke analogues:
498 composition, optical properties and growth kinetics, *J. Atmos. and Sol. Terr. Phys.*, *68*(18),
499 2182-2202

500 Saunders, R. W., and J. M. C. Plane (2011), A photo-chemical method for the production of
501 olivine nanoparticles as cosmic dust analogues, *Icarus*, *212*(1), 373-382

Siskind, D. E., M. H. Stevens, C. R. Englert, and M. G. Mlynczak (2013), Comparison of a photochemical model with observations of mesospheric hydroxyl and ozone, *J. Geophys. Res.*, *118*(1), 195-207

Stone, D., and D. M. Rowley (2005), Kinetics of the gas phase HO_2 self-reaction: Effects of temperature, pressure, water and methanol vapours, *Phys.Chem. Chem. Phys.*, *7*(10), 2156-2163

Stone, D., L. K. Whalley, and D. E. Heard (2012), Tropospheric OH and HO_2 radicals: field measurements and model comparisons, *Chem. Soc. Rev.*, *41*(19), 6348-6404

Summers, M. E., and D. E. Siskind (1999), Surface recombination of O and H_2 on meteoric dust as a source of mesospheric water vapor, *Geophys. Res. Lett.*, *26*(13), 1837-1840

Thornton, J., and J. P. D. Abbatt (2005), Measurements of HO_2 uptake to aqueous aerosol: Mass accommodation coefficients and net reactive loss, *J. Geophys. Res.*, *110*, art. no. D08309

Waters, J. W., et al. (2006), The Earth observing system microwave limb sounder (EOS MLS) on the aura Satellite, *IEEE Trans. Geosci. Remote Sensing*, *44*(5), 1075-1092

Table Headings

Table 1 Values of γ measured in this study.

Tables

Table 1 Values of γ measured in this study.

MSP analogue	RH / %	Measured γ	R^2 (see Fig. 4 a)
Forsterite	11.6	$(4.3 \pm 0.4) \times 10^{-3}$	0.953
Olivine	10.0	$(6.9 \pm 1.2) \times 10^{-2}$	0.985
Fayalite	9.9	$(7.3 \pm 0.4) \times 10^{-2}$	0.945

Figure Captions

Figure 1 Schematic diagram of the experimental system. Abbreviated components: Condensation Particle Counter (CPC), Mass Flow Controller (MFC) and Photo-Multiplier Tube (PMT).

Figure 2 Measured size distribution of fayalite at 9.9 % RH, normalised to the peak of a log normal fit to the distribution. Ten individual measurements are shown in grey with the mean in black and a log normal fit (mean and standard deviation of 368 nm and 0.680 respectively) to the size distribution in red.

Figure 3 (a) Example plot showing the anti-correlation of HO_2 signal to number concentration of fayalite MSP analogue particles (at 9.9 % RH with a residence time of 20.6 s). (b) Example plot showing the HO_2 signal variation with fayalite aerosol number concentration, also at 9.9 % RH for three fixed contact times as shown in the legend. Full experimental conditions are given in the text. Means and standard deviations of three condensation particle counter and FAGE measurements are shown (as points and error bars, respectively).

Figure 4 (a) Plot of the dimensionless quantity $0.25\gamma_{obs}wA_dt$ as a function of reaction time for uptake of HO_2 onto fayalite at a RH = 9.9%. The linear least-squares fit to these point yields $0.25\gamma_{obs}wA_d$ as the gradient, $(6.3 \pm 1.4) \times 10^{-6}$ in this case, from which $\gamma_{obs} = (7.3 \pm 0.4) \times 10^{-2}$ was obtained. The intercept of the fit at $t = 0$ ($(2.3 \pm 1.8) \times 10^{-5}$) suggests a higher gradient and hence a higher uptake coefficient occurring in the first few seconds of contact between the HO_2 and fayalite aerosols. The error bars represent 2 standard deviations in the individual exponential fits, examples of which are given in Figure 3(b). (b) Plot of γ_{obs} determined from a straight line from the origin to each point in panel (a), demonstrating that over time γ_{obs} decreases toward the value obtained from the straight line fit shown in panel (a).

Figure 5 Electronic structure calculations at the B3LYP/6-311+g(2d,p) level of theory with enthalpies in kJ mol^{-1} in brackets: (a) HO_2 uptake on an exposed Fe atom on the olivine surface leads to a chemisorbed adduct (b); a second HO_2 can now abstract the adsorbed H atom via transition state (c) to form (d), where O_2 is bound to the Fe atom, which can then be displaced by a further HO_2 to yield (b). When HO_2 adds to an exposed Mg atom, chemisorption leads to the very stable structure (e).

Figure 6 (a) Zonal average HO_2 mixing ratio (ppbv) as measured by the Microwave Limb Sounder (MLS) for January 2005. (b) Zonal average HO_2 mixing ratio (ppbv) as predicted by WACCM-CARMA simulations using specified dynamics for January 2005, from a control simulation with no heterogeneous uptake of HO_2. The colour bar applies to both panels but

should be interpreted with caution since a nonlinear colour scaling has been used to display the full range of the data.

Figure 7 (a) Percentage difference in HO_2 volume mixing ratio between a WACCM-CARMA simulation with γ = 0.2 and a 'control' simulation with γ = 0. (b) % RH in the control simulation. (c) Available surface area ($\mu m^2\ cm^{-3}$) of MSP from the WACCM-CARMA control simulation. Data for all panels is zonally averaged at 80^o S. Colour bars are included to aid the reader, however these should be treated with caution since nonlinear colour scaling has been used to accentuate features in each panel.

Figure 8 Percentage difference in HO_2 volume mixing ratio between the two model runs as a function of latitude for June 2009. The colour bar should be interpreted with caution as nonlinear colour scaling has been used to accentuate features in the plot.

572

Figure 1.

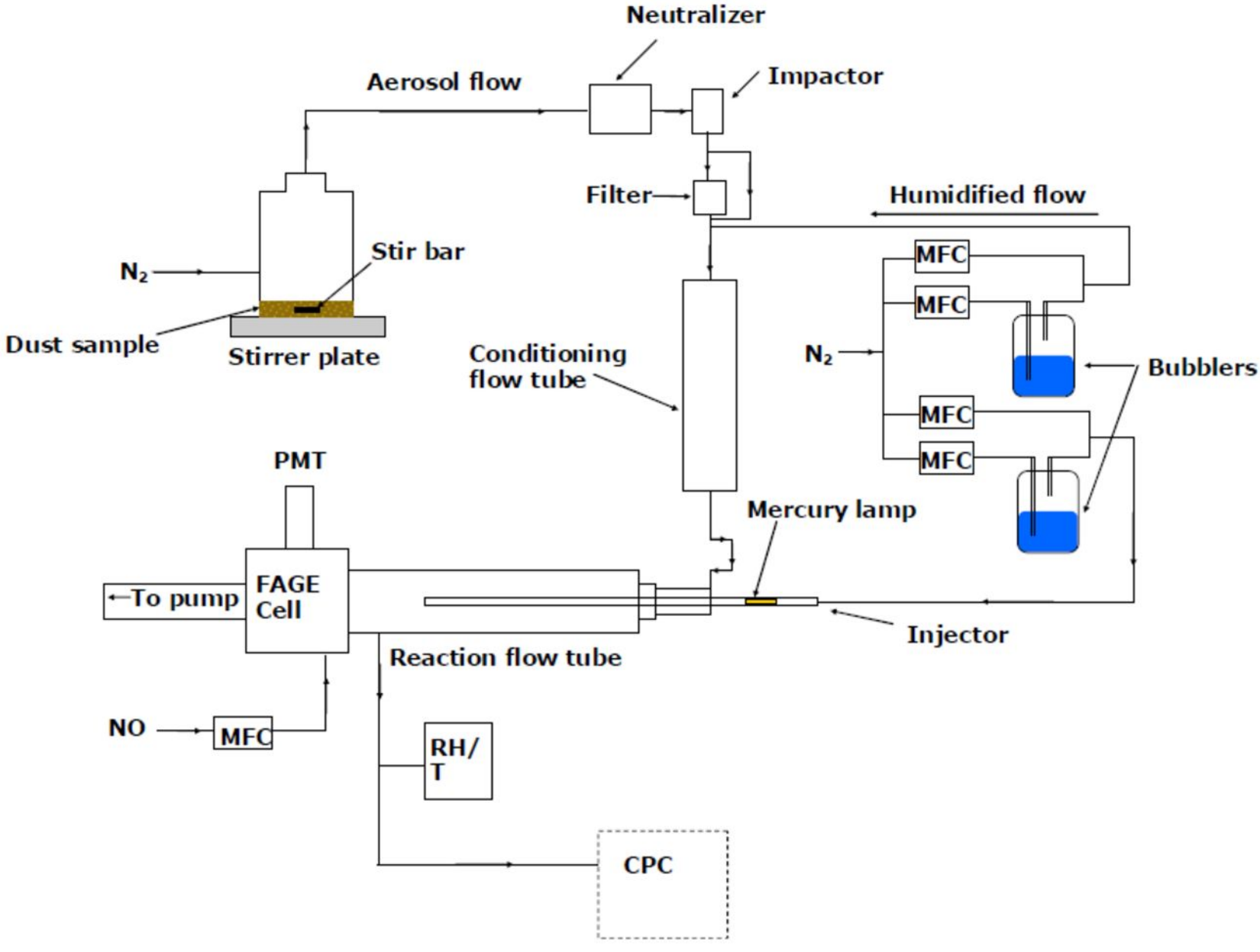
Neutralizer
Aerosol flow
Impactor
Filter
Humidified flow
MFC
MFC
N_2
Stir bar
Dust sample
Stirrer plate
Conditioning flow tube
Bubblers
MFC
MFC
PMT
Mercury lamp
To pump
FAGE Cell
Injector
Reaction flow tube
NO
MFC
RH/ T
CPC

Figure 2.

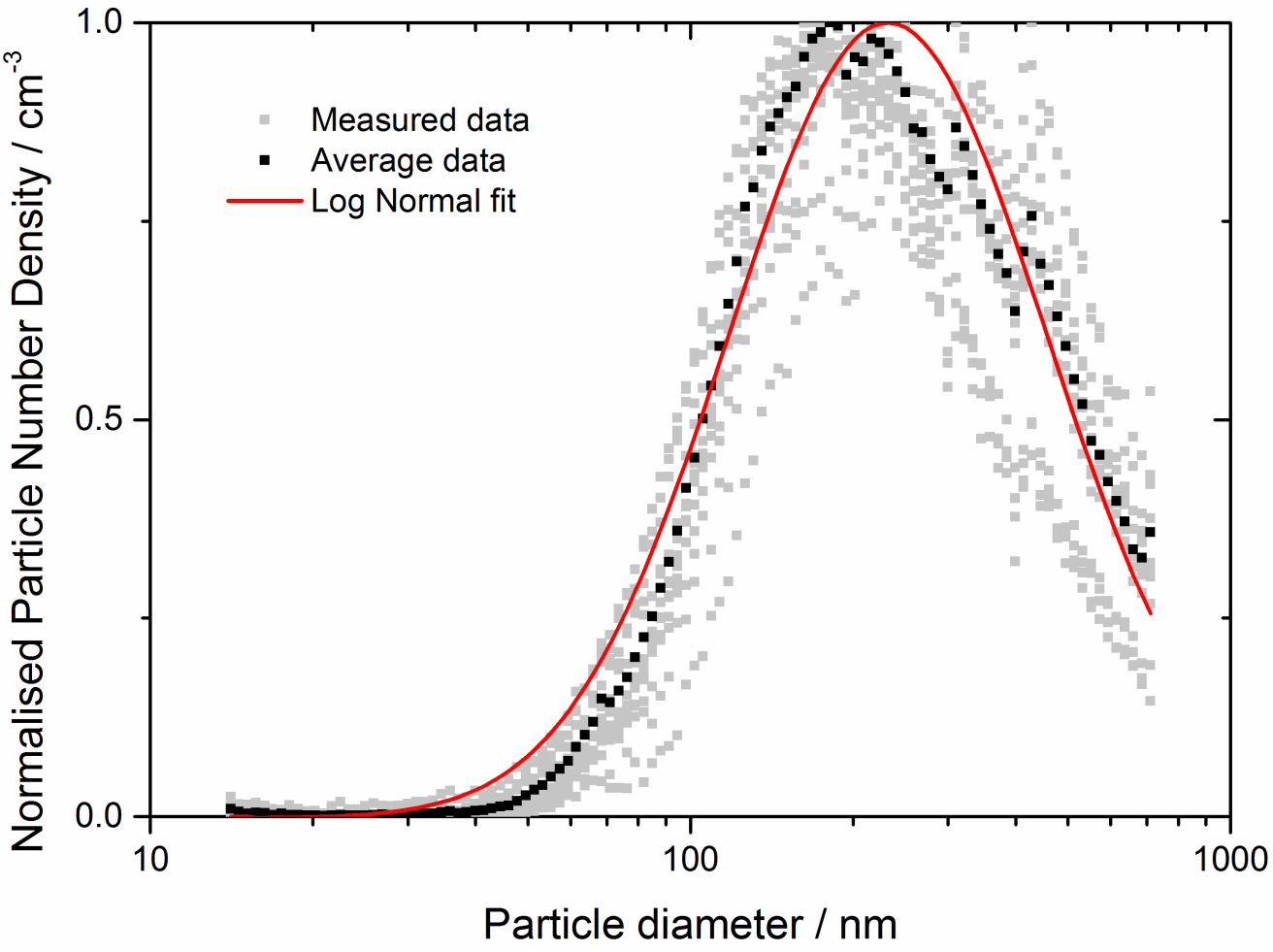
Measured data
Average data
Log Normal fit
Normalised Particle Number Density / cm-3
Particle diameter / nm
1.0
0.5
0.0
10
100
1000

Figure 3.

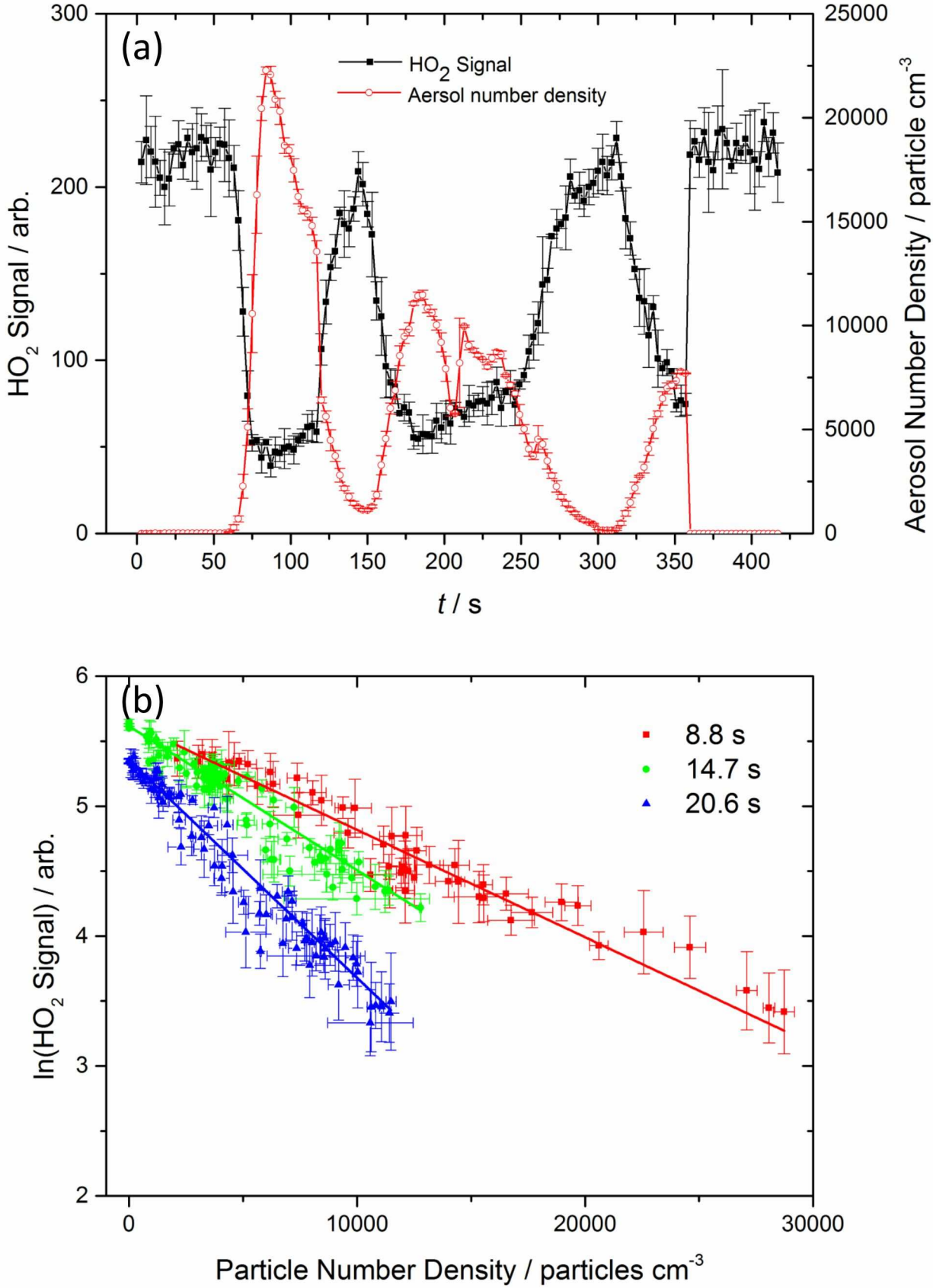
(a)
HO2 Signal
Aersol number density
HO2 Signal / arb.
Aerosol Number Density / particle cm-3
t / s
(b)
8.8 s
14.7 s
20.6 s
ln(HO2 Signal) / arb.
Particle Number Density / particles cm-3

Figure 4.

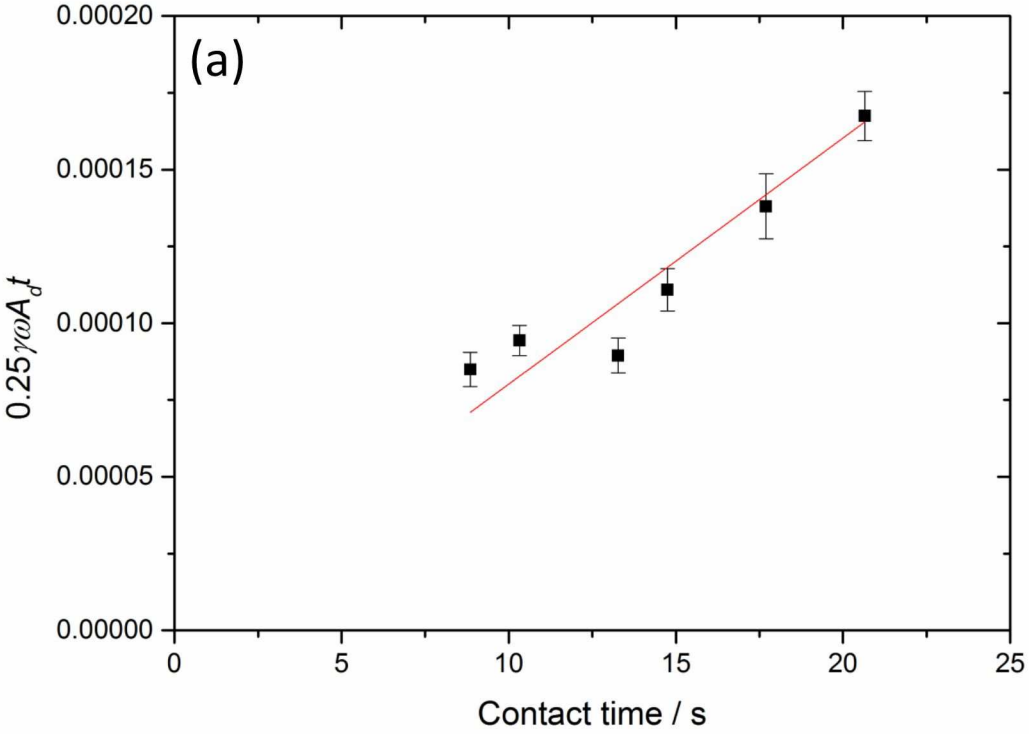
(a)
0.00020
0.00015
0.00010
0.00005
0.00000
$0.25\gamma\omega A_d t$
0
5
10
15
20
25
Contact time / s

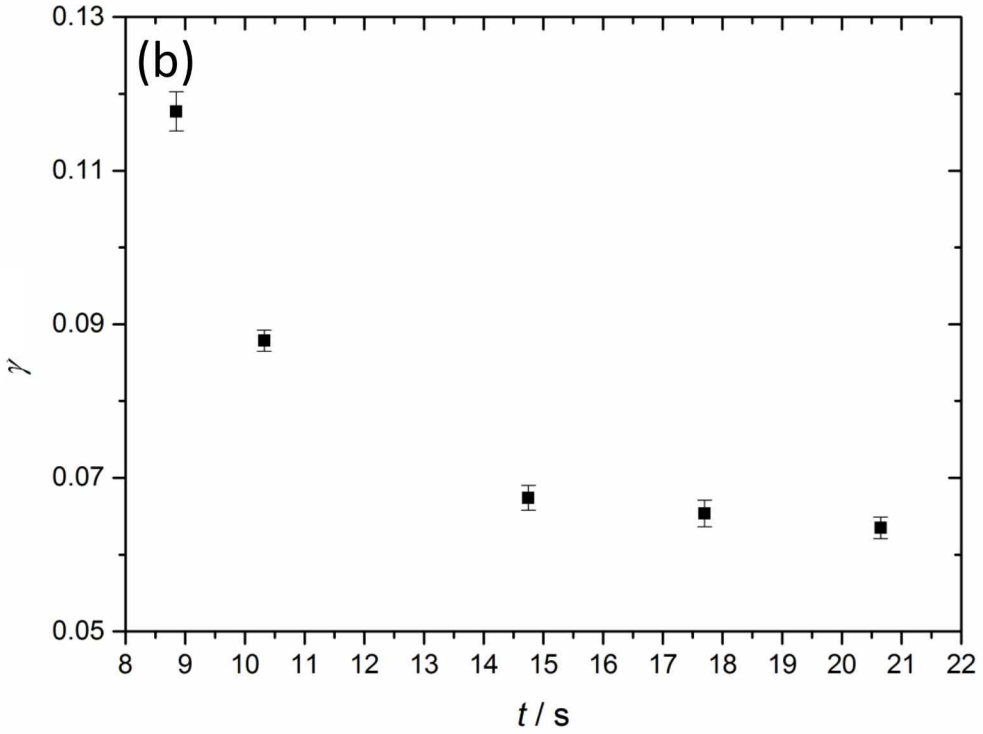
(b)
0.13
0.11
0.09
0.07
0.05
γ
8
9
10
11
12
13
14
15
16
17
18
19
20
21
22
t / s

Figure 5.

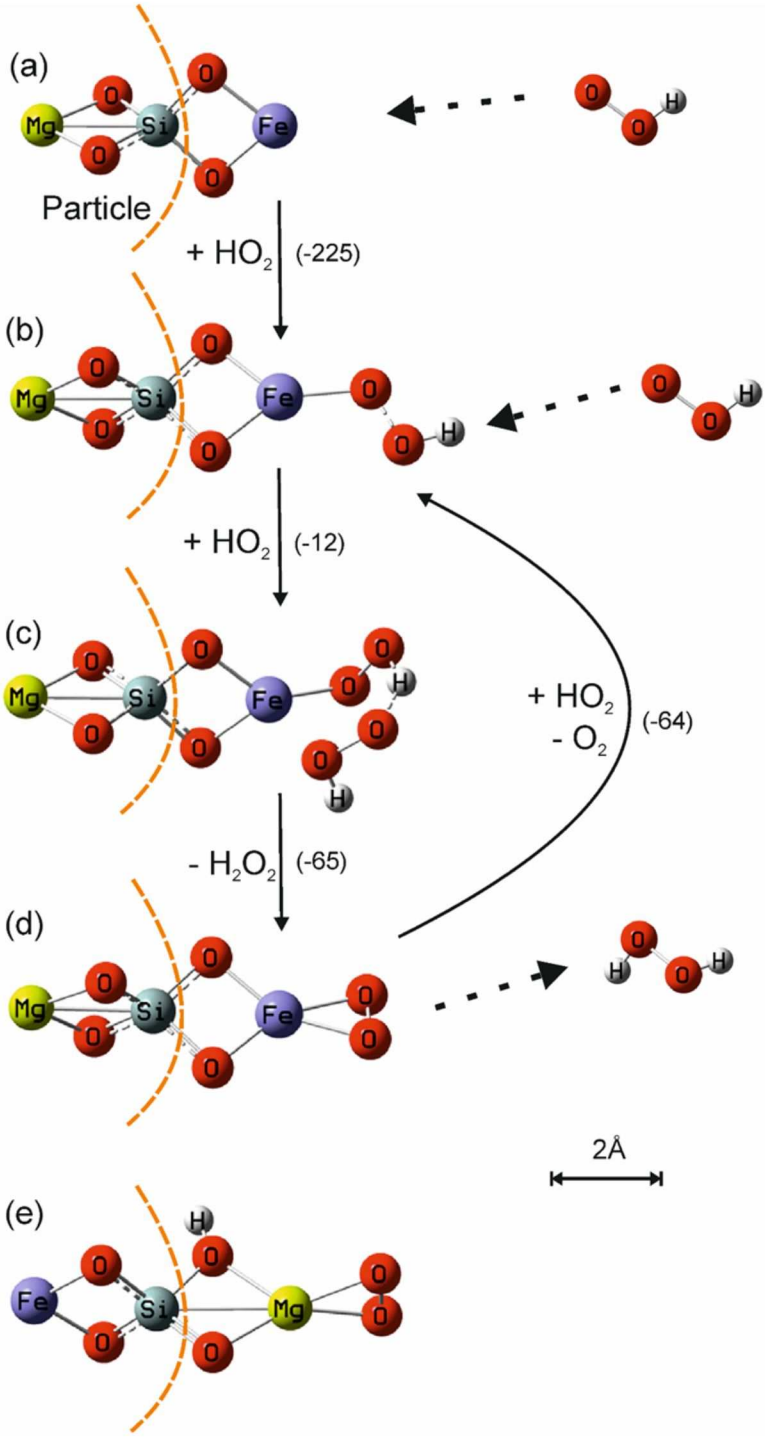
(a)
Particle
+ HO2
(-225)
(b)
+ HO2
(-12)
(c)
+ HO2
- O2
(-64)
- H2O2
(-65)
(d)
2Å
(e)

Figure 6.

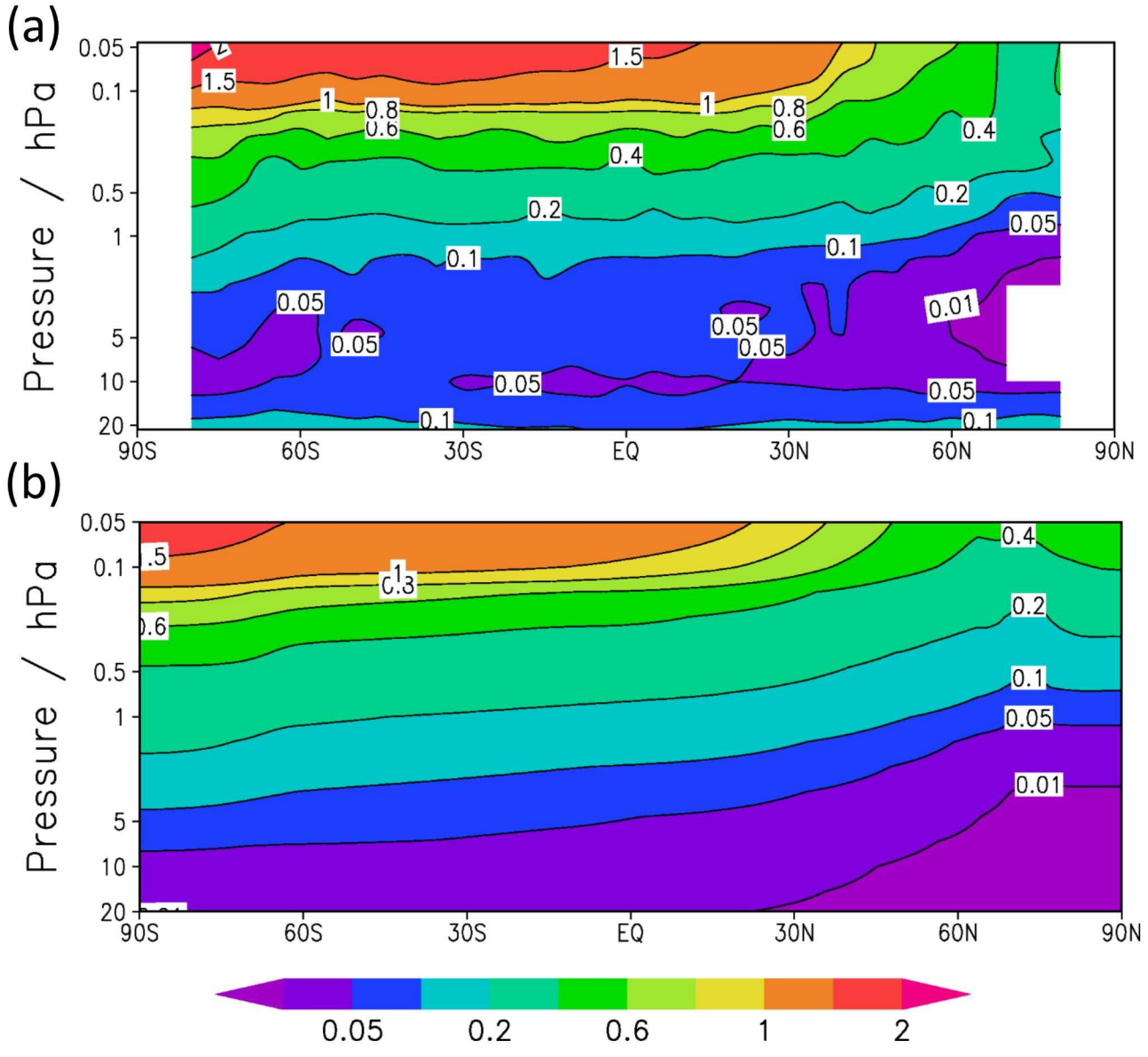
(a)
Pressure / hPa
0.05
0.1
0.5
1
5
10
20
90S
60S
30S
EQ
30N
60N
90N
1.5
1
0.8
0.6
0.4
0.2
0.1
0.05
0.01
(b)
Pressure / hPa
0.05
0.2
0.6
1
2

Figure 7.

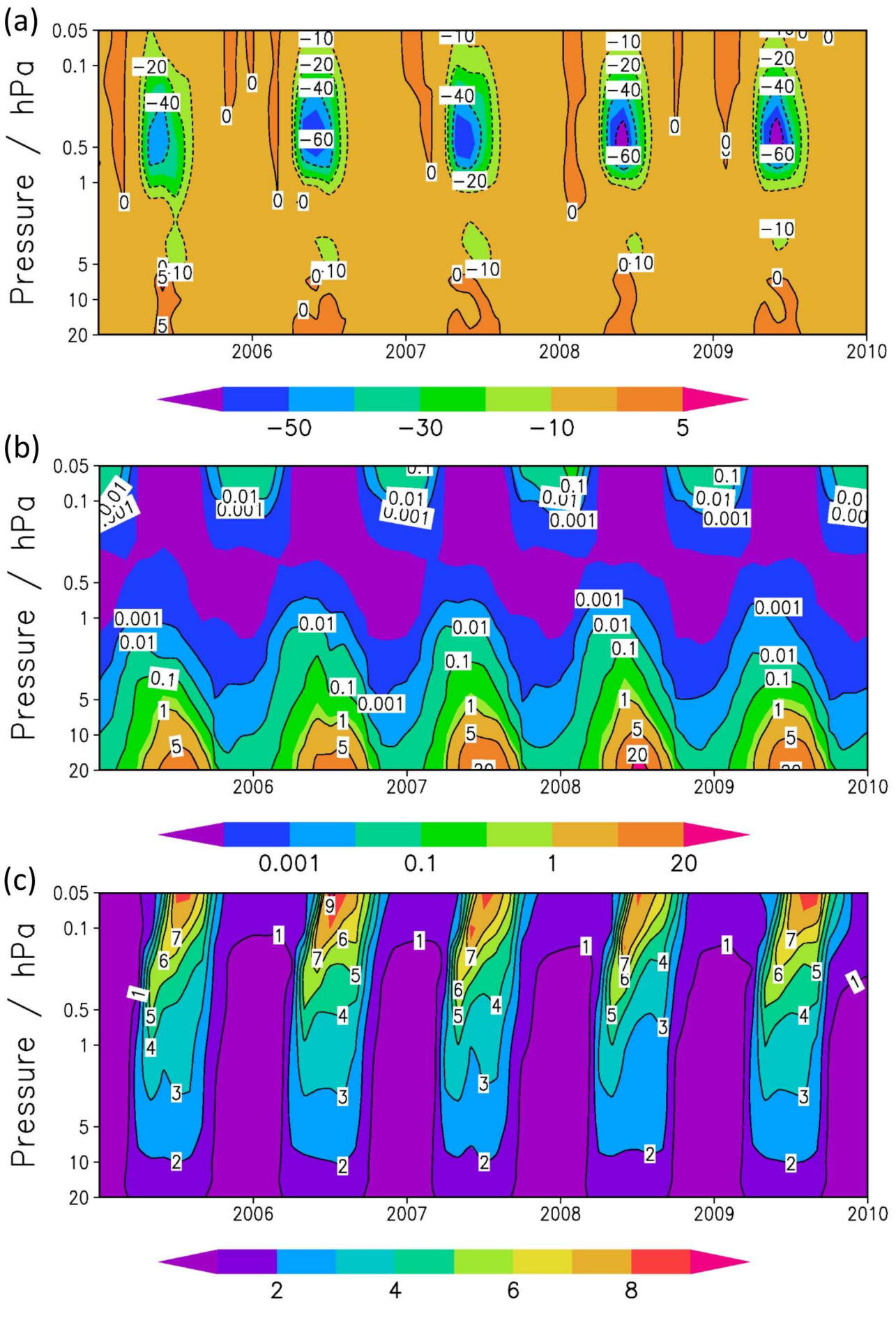
(a)
Pressure / hPa
0.05
0.1
0.5
1
5
10
20
2006
2007
2008
2009
2010
−50
−30
−10
5
(b)
Pressure / hPa
0.001
0.01
0.1
1
5
20
(c)
Pressure / hPa
2
4
6
8

Figure 8.

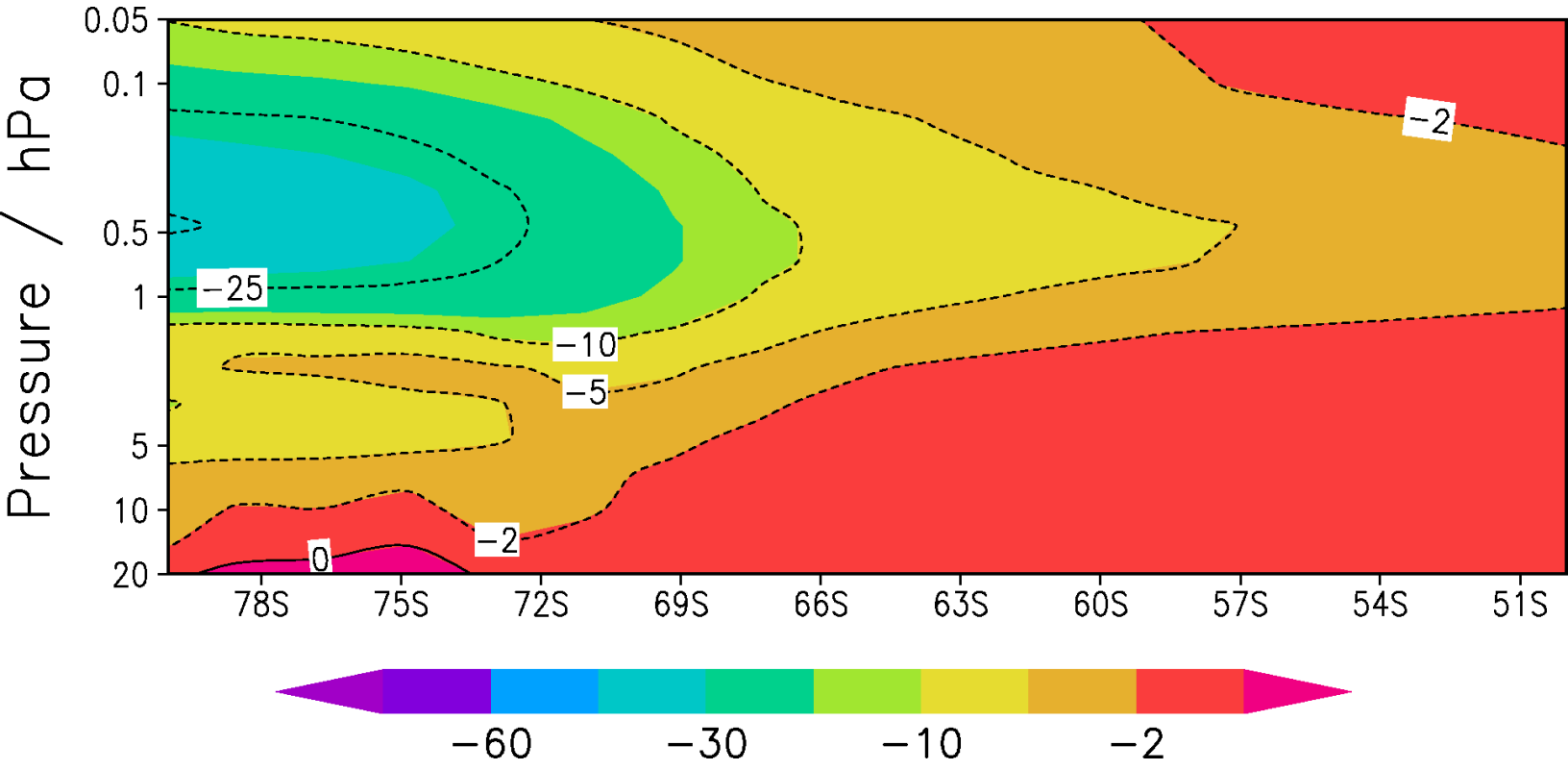
Pressure / hPa
0.05
0.1
0.5
1
5
10
20
78S
75S
72S
69S
66S
63S
60S
57S
54S
51S
−25
−10
−5
−2
0
−2
−60
−30
−10
−2